PAPER

Check for updates

Acid-assisted self-assembly of pyrene-capped tyrosine ruptures lysosomes to induce cancer cell apoptosis†

Jing Li,[ab] Jiaqi Song,[c] Liang Shao,[c] Xianpeng Zhang, [ID][c] Ziyi Wang,[ab] Guanying Li, [ID]*[c] Jiansheng Wang*[ab] and Jia Zhang*[b]

Induced lysosomal membrane permeabilization (LMP) by peptide self-assembly has emerged as an effective platform for lysosome-targeted cancer therapy. In this study, we shift this strategical paradigm and present an innovative approach to LMP induction through amino acid-based self-assembly. Pyrene-capped tyrosine (**Py-Tyr**), as a proof-of-concept molecule, is designed with acidity-responsive self-assembly. Under acidic conditions (pH 4), **Py-Tyr** is protonated with reduced charge repulsion, and self-assembles into micrometer-scaled aggregates, which exceed the biological size of lysosomes. Cell experiments showed that **Py-Tyr** specifically accumulates in lysosomes and induces lysosome rupture, leading to the release of cathepsin B into the cytoplasm for subsequent apoptosis activation in cancer cells. This study capitalizes on the concept of amino acid assembly for efficient LMP induction, providing a simple and versatile platform for precise and effective therapeutic interventions in cancer therapy.
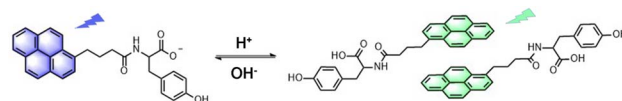
Introduction

In cancer cells, lysosomes undergo several alterations,[1] such as enhanced lysosomal biogenesis, increased lysosomal enzyme activity, and altered lysosomal pH. These alterations on lysosomal function have profound effects on cancer cell survival, invasion, and resistance to therapy. On the other hand, they also present a unique vulnerability that can be exploited for therapeutic intervention.[2,3] Targeting lysosomal membrane permeability and integrity has been demonstrated as one of the efficient strategies in lysosome-targeting therapy.[4,5] Specifically, lysosomal membrane permeabilization (LMP) occurs under stress conditions, and leads to the leakage of lysosomal contents into the cytosol, triggering amplified stress response and cell death. For example, destabilization of the constitutive protein of lysosomal membrane, LAMP-2, could induce LMP.[6] A synthetic platform could provide a simple and effective method for LMP induction, offering promising alternatives for lysosome-targeting therapy.

Molecular self-assembly is a bottom-up building process to obtain large size structures. Oligopeptide-based building blocks such as diphenylalanine have been widely used for constructing self-assembled nanostructures, and developed as functional materials.[7] By regulating the self-assembly processes or stimuli, peptide assembly can occur specifically on the pericellular space,[8] on the cell membrane,[9,10] or in the cytosol,[11,12] generating subcellular organelle-targeting bio-nanointerfaces to interfere with specific targets or cause stress response leading to cell death. Recently, lysosome-targeting peptide self-assemblies have also been successfully developed.[13–17] Although this approach has paved the way in lysosome targeted therapy, it faces challenges in achieving optimal specificity and control over lysosomal dynamics.

In this study we present a paradigm shift in strategy by designing amino acid-based self-assembly. Tyrosine (Tyr) as an essential aromatic amino acid in the nature, can self-assemble into well-organized nanostructure.[18,19] However, at acidic pH, Tyr is positively charged and could not self-assemble. To actively utilize the self-assembly of Tyr and explore its capability for LMP induction, we incorporate a pyrene moiety on its N-terminal to obtain the designed molecule pyrene-1-butanoyl tyrosine (**Py-Tyr**, as shown in Scheme 1). **Py-Tyr** introduces

The Second Clinical Medical School, Shaanxi University of Chinese Medicine, Xianyang Shaanxi, China. E-mail: wangjsh@xjtu.edu.cn

The Department of Thoracic Surgery, The First Affiliated Hospital of Xi'an Jiaotong University, Xi'an Jiaotong University, Xi'an Shaanxi, China. E-mail: zhangjiaxjtu@xjtu.edu.cn

Department of Biophysics, School of Basic Medical Sciences, Xi'an Jiaotong University, Xi'an Shaanxi, China. E-mail: guanyingli@xjtu.edu.cn

† Electronic supplementary information (ESI) available. See DOI: https://doi.org/10.1039/d4ra01328j

Scheme 1 Chemical structure of **Py-Tyr** at deprotonated state, and the proposed dimer structure of [**Py-Tyr**]$_2$ at protonated state, which further assembles to form large-scaled structures in lysosomes for LMP induction.

a novel synthetic platform advancing the self-assembling capabilities of tyrosine for efficient LMP induction. This controlled assembly process, responding specifically to lysosomal acidity, ensures precise targeting and optimized functionality for LMP-mediated cancer therapy.

Results and discussions

Molecular design

Py-Tyr possesses several unique features tailored for efficient LMP induction: (1) N-capping of tyrosine blocks the protonation at acidic condition and reduces its charge repulsion; (2) the addition of pyrene ring offering extensional π–π stacking facilitates the self-assembly; (3) self-assembly of **Py-Tyr** results in a higher apparent pK_a than the theoretical pK_a (3.5),[20] aligning strategically with the acidic environment of lysosomes; (4) the presence of pyrene moiety enables the monitoring of **Py-Tyr**'s self-assembly and cellular location through excimer emission.[21] (5) low molecular weight of **Py-Pyr** compared to self-assembling peptides enhances cellular uptake and specificity of lysosome-targeting. Therefore, **Py-Tyr** emerges as a lead molecule capitalized on the amino acid self-assembly for targeting the distinct vulnerabilities of cancer cell lysosomes.

pH-dependent self-assembly of Py-Tyr

Py-Tyr was synthesized by solid phase synthesis and characterized by mass spectrum and ¹H NMR (Fig. S1 and 2†). Molecular geometries of **Py-Tyr** and its deprotonated form (**Py-Tyr⁻**) were optimized using Gaussian-09 software.[22] The results showed that deprotonated **Py-Tyr⁻** exhibited a compact molecular conformation, where the pyrene ring and the phenol ring of Tyr residue were almost parallel (Fig. 1a). Under acidic condition, however, the conformation of **Py-Tyr** was extended, where the pyrene ring was intersecting against the phenol ring with a dihedral angle of 100° (Fig. 1b). The conformational difference illustrated that **Py-Tyr** under acidic condition has an extra direction of intermolecular interactions. A bimolecular geometry was also optimized and demonstrated that **[Py-Tyr]₂** dimer exhibited a tail-to-tail packing mode. The planar distance between two adjacent pyrene planes of 4.97 Å (Fig. 1c),

indicating strong intermolecular interaction for emitting excimer fluorescence.

Therefore, we explored the pH-dependent self-assembly of **Py-Tyr** using emission spectroscopy. Concentration-dependent emission spectra of **Py-Tyr** at different pH conditions were recorded (Fig. S3†) and normalized based on the intensity of monomer fluorescent at 375 nm (Fig. S4†). **Py-Tyr** exhibited concentration-dependent excimer emission at 458 nm, which is not surprising. As shown in Fig. 2a, at physiological pH (7.4), **Py-Tyr** only emitted excimer fluorescence at high concentration (200 μM). At pH 4.0, however, excimer fluorescence could be observed at 25 μM, indicating strong intermolecular interaction of **Py-Tyr** at acidic condition. The intensity ratio between excimer fluorescence and monomer fluorescence of **Py-Tyr** was summarized and visualized using a heatmap (Fig. 2b). The higher ratio of I_{458}/I_{375}, the stronger self-assembly of **Py-Tyr**. At each pH value, the I_{458}/I_{375} ratio of **Py-Tyr** increased when increasing its concentration. Under the same concentration, the I_{458}/I_{375} ratio also increased when the media tuned acidic. The results clearly demonstrated a pH-dependent and concentration-dependent manner of **Py-Tyr** self-assembly. The UV-vis spectra of **Py-Tyr** at different pH values were also measured (Fig. S5†) and suggested that **Py-Tyr** could self-assemble when pH was lower than 5.

We then measured the hydrodynamic diameters of self-assembled structures of **Py-Tyr** at different pH values using dynamic light scattering (DLS). The results (Fig. 2c) showed that 100 μM of **Py-Tyr** could form nanoscale aggregates with an average diameter of 110 nm at pH 8.0. The hydrodynamic diameters of self-assembled structures slowly increased when the pH values varied from 8.0 to 5.5. At pH 5.0, the hydrodynamic diameter sharply increased to 736 nm. Micro-scaled aggregates could be observed under pH 4.0, as indicated by the hydrodynamic diameter at pH 4.0, probably because it was lower than the apparent pK_a value. Zeta potential measurements (Fig. 2d) indicated that **Py-Tyr** carried negative charge, displaying a surface potential of −35.3 mV at pH 8.0. However, at pH 4.0, the surface potential significantly increases to −18.9 mV. These findings implied that the self-assembly behavior of **Py-Tyr** is influenced by pH values.
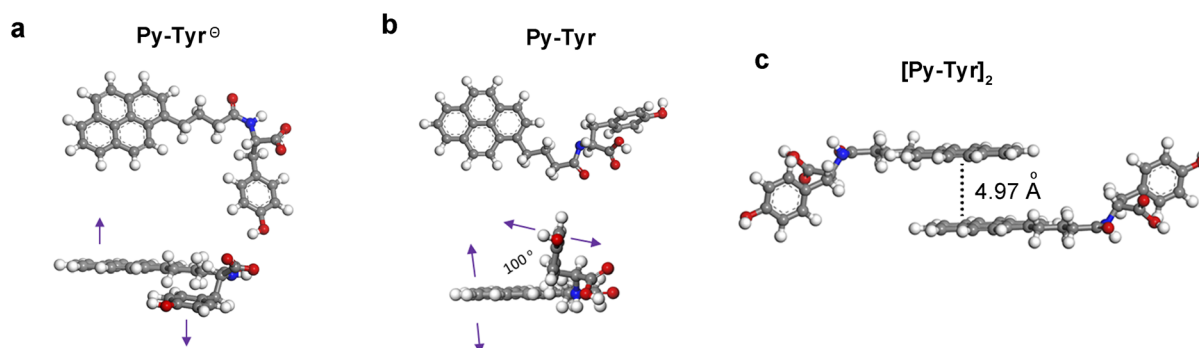

Fig. 1 Optimized geometries of deprotonated Py-Tyr⁻ (a) protonated Py-Tyr (b) and its dimer [Py-Tyr]₂ (c). Arrows indicate potential π–π interactions for self-assembly.
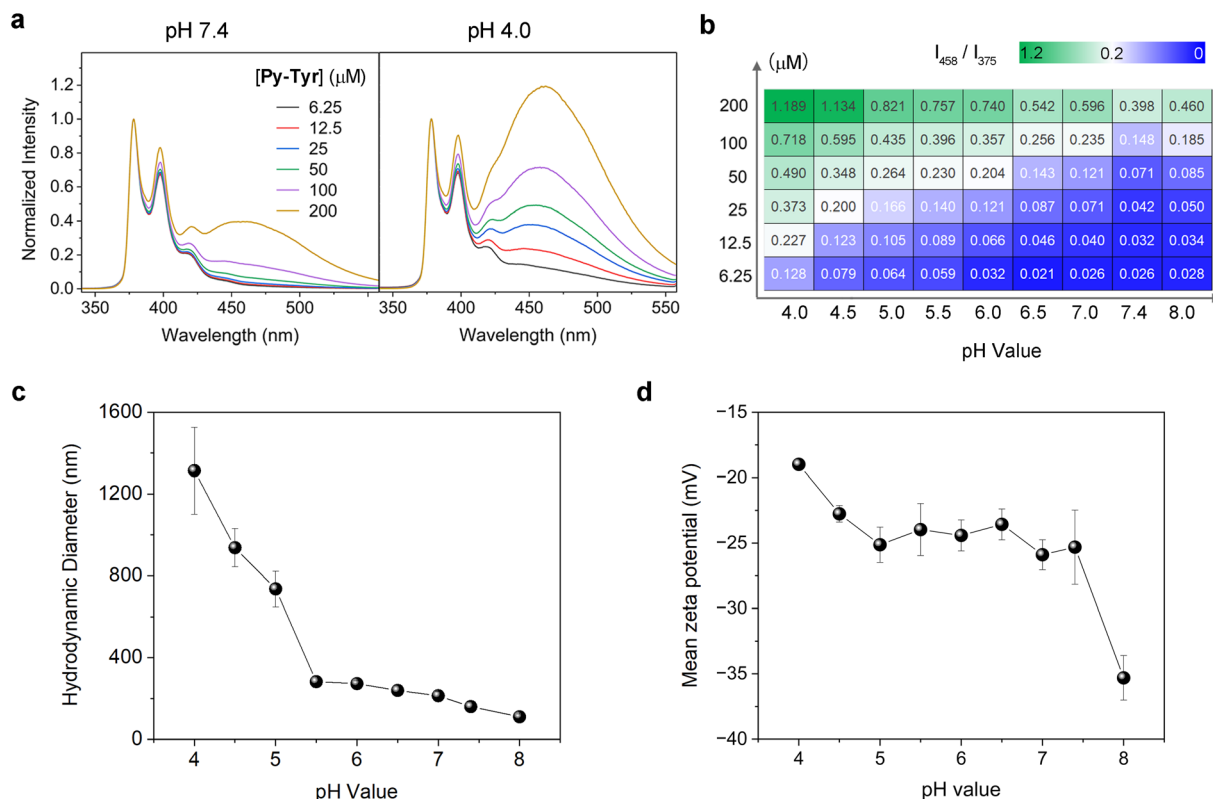
Fig. 2 pH-dependent self-assembly of **Py-Tyr**. (a) Normalized emission spectra of **Py-Tyr** in citrate–phosphate buffer under pH 7.4 or pH 4.0. The fluorescence intensity at 375 nm was normalized to 1.0, respectively. The concentration of **Py-Tyr** varied from 200, 100, 50, 25, 12.5 and 6.25 μM. $\lambda_{ex} = 342$ nm. (b) Heatmap of the emission intensity ratio (I_{458}/I_{375}) of **Py-Tyr** under various concentrations and pH values. Three colors were mapped with the setting of: blue, $I_{458}/I_{375} = 0$; white, $I_{458}/I_{375} = 0.2$; green, $I_{458}/I_{375} = 1.2$, respectively. (c) Hydrodynamic diameters of 100 μM **Py-Tyr** assemblies in citrate–phosphate buffer under various pH values. (d) Zeta-potentials of 100 μM **Py-Tyr** assemblies in citrate–phosphate buffer under various pH values.

The morphologies of **Py-Tyr** self-assembled structures were examined using transmission electron microscopy (TEM). Under pH 4.0 **Py-Tyr** formed nanoparticles (Fig. 3a) with an average diameter of 5.3 ± 1.8 nm (Fig. 3c), which further clustered into large aggregates. Small particles of **Py-Tyr** also aggregated into large cluster under lysosomal lumen pH 4.5 (Fig. S6†). In contrast, **Py-Tyr** formed relatively small nanoparticles in PBS buffer (pH 7.4) with an average diameter of 2.4 ± 0.8 nm, and no large particle clusters could be observed (Fig. 3b). The size difference of single particle under pH 4 and under pH 7.4 could be attributed to their molecular conformations (Fig. 1).

Time-dependent self-assembly of Py-Tyr

After ageing under pH 4.0, the nanoparticles continuously self-assembled to form large aggregates. The growing sizes were monitored. As shown in Fig. 3d, the size of **Py-Tyr** self-assembled particles under pH 4.0 significantly increased over 10 μm after 4 h, and exceeded 30 μm after 24 h. However, at pH 7.4, the size of **Py-Tyr** self-assembled particles remained relatively stable, and no significant aggregation was observed even with extended time (Fig. 3d). This growing size of **Py-Tyr** self-assembled particles under pH 4.0 was further confirmed by TEM observation (Fig. 3e). In contrast, TEM images of **Py-Tyr**

self-assembled particles under pH 7.4 showed small particle cluster (Fig. 3f). To simulate the self-assembly **Py-Tyr** under lysosomal environment, we monitored the ageing of **Py-Tyr** under pH 4.5 that is closed to the lysosomal acidity. Under pH 4.5, compact aggregates of **Py-Tyr** assemblies could be observed after 2 h, which continued growing to form large aggregates. Contrary, **Py-Tyr** slowly aggregated into particle clusters under pH physiological pH 7.4 (Fig. S7†). These findings confirmed the acid-assist enlargement of **Py-Tyr** aggregates, inspiring us to further investigate its LMP induction in cancer cells.

Lysosome accumulation of Py-Tyr self-assembly

To assess the feasibility of **Py-Tyr**-induced LMP, we first tested the cytotoxicity of **Py-Tyr** assemblies against cancer cells, including lung cancer A549 cells, liver cancer HepG2 cells and osteosarcoma Saos2 cells using CCK-8 assay. Fig. 4 showed a concentration-dependent cytotoxic effect of **Py-Tyr** against these cancer cells. At 100 μM, **Py-Tyr** exhibited completely cancer killing ability against these cancer cells. This phenomenon was in line with the concentration-dependent self-assembling behaviors (Fig. 2a and b), implying potential LMP induction of **Py-Tyr** assemblies in cancer cells. Among these cancer cells, **Py-Tyr** showed the highest cytotoxicity against A549 cells with an IC50 value at 71 μM, which was chosen as the
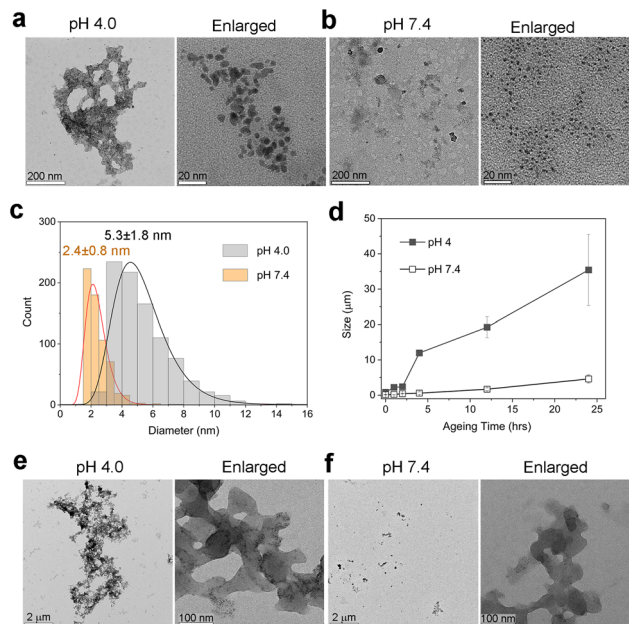
Fig. 3 Time-dependent self-assembly of **Py-Tyr**. (a and b) TEM images of freshly prepared 100 μM **Py-Tyr** assemblies at pH 4.0 (a) or at pH 7.4 (b). (c) Quantification of particles sizes of 100 μM **Py-Tyr** assemblies at pH 4.0 or at pH 7.4 in the TEM images and the histogram distribution. (d) Hydrodynamic diameters of 100 μM **Py-Tyr** assemblies at pH 4.0 or pH 7.4 after ageing for 1, 2, 4, 12, and 24 h (e and f) TEM images of 100 μM **Py-Tyr** assemblies at pH 4.0 (e) or at pH 7.4 (f) after ageing for 24 h.
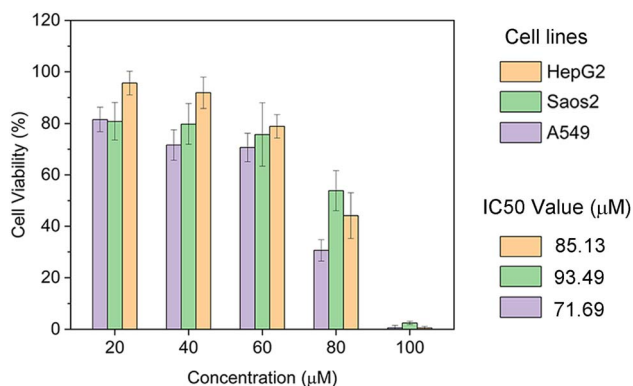

Fig. 4 Cell viability of HepG2, Saos2 and A549 cells treated with 20, 40, 60, 80, 100 μM **Py-Tyr** for 48 h, mean ± SD, $n = 5$.

model cell line for studying the LMP induction of **Py-Tyr** assemblies.

Freshly prepared **Py-Tyr** formed small particles under pH 7.4 (Fig. 2c and 3b), which could be internalized through endocytic pathways.[23,24] During maturation of endosomes, the acidification increases and reaches pH 4.5–5.0 in the lysosomes. Considering self-assembly of **Py-Tyr** is pH-dependent, it is reasonable to hypothesize that during the endo/lysosomal internalization pathway, increasing acidification triggers the aggregation of **Py-Tyr** self-assemblies into large and micrometre-scaled assemblies, eventually trapping them in the lysosomes (Fig. 5a). Benefitting from the intrinsic fluorescence
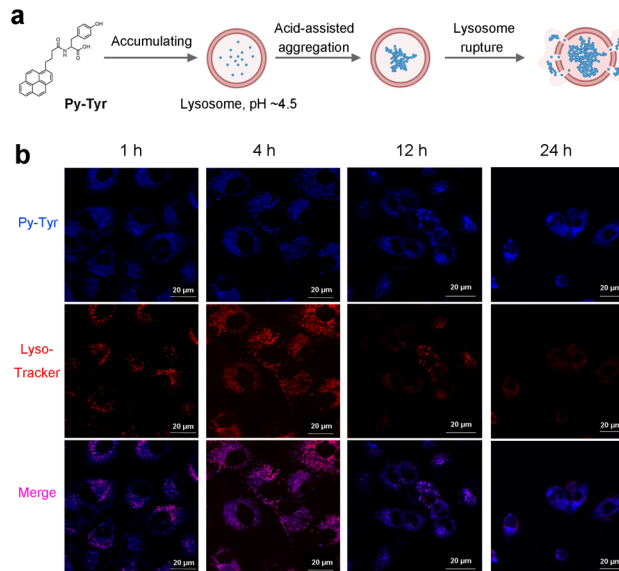

Fig. 5 Lysosome accumulation of **Py-Tyr**. (a) Schematic illustration of lysosome accumulation, aggregation, and induced lysosome rupture of **Py-Tyr** assemblies. (b) CLSM images of A549 cells treated with 70 μM **Py-Tyr** (blue) for 1, 4, 12, and 24 h. Cells were co-stained with Lyso-Tracker Red DND-99 (Lyso-Tracker, red).

of pyrene fluorophore, we managed to monitor the process of targeting and accumulation of **Py-Tyr** assemblies within the lysosome by confocal laser scanning microscope (CLSM). As shown in Fig. 5b, A549 cells were treated with **Py-Tyr** for desired time and then co-stained with a commercial lysosome-specific dye Lyso-Tracker Red DND-99. After 20 min treatment of **Py-Tyr**, fluorescence signal appearing on the cell membrane was detected (Fig. S8†); meanwhile, fluorescence signal non-specifically locating in the cytosols was also detected, indicating cellular uptake of **Py-Tyr**. As the incubation time extended to 1 h (Fig. 5b) and 2 h (Fig. S8†), A549 cells showed bright intracellular fluorescence partially co-localizing with lysosomes, suggesting internalization of **Py-Tyr**. After 4 h incubation, the fluorescence of **Py-Tyr** dominantly colocalized with the Lyso-Tracker, revealing that specific lysosomal accumulation of **Py-Tyr** at 4 h.

A long incubation time was performed to investigate the alteration of **Py-Tyr** assemblies on lysosomes. At 12 h, CLSM images (Fig. 5b) showed that condensed spots of **Py-Tyr** fluorescence in bright intensity remained in the lysosomes, while the rest appeared in the cytosols, suggesting **Py-Tyr** assemblies escaped from the lysosomes. It should also be noted that intensity of Lyso-Tracker significantly decreased, implying the disturbance of **Py-Tyr** on the lysosomal environment. At 24 h, however, Lyso-Tracker fluorescence vanished, accompanied with the highly condensed fluorescence of **Py-Tyr** in micrometer-scaled spots which exceeded the biological sizes of lysosomes. These results revealed that acid milieu of lysosomes facilitated the continuous assembly of **Py-Tyr** into large-scaled assembled structures, eventually leading to LMP induction and lysosome rupture.

Lysosomes rupture induces cancer cell apoptosis

Lysosomes contain about 50 different hydrolases. Lysosomes rupture induced by **Py-Tyr** assemblies under acid stimuli potentially releases these hydrolases into the cytoplasm. The massive and uncontrolled leakage of lysosomal contents triggers the activation of apoptotic signalling cascades,[25,26] contributing to irreversible cell damage (Fig. 6a). To verify, we fluorescently stained cathepsin B, one of the main hydrolases in lysosomes,[27] and tracked its cellular localization in A549 cells. As shown in Fig. 6b, cathepsin B was restricted in the lysosomes without **Py-Tyr** treatment. Upon the treatment with **Py-Tyr** for 24 h, decreased intensity of LysoTrakcer implied the lysosome damages induced by **Py-Tyr**. Cathepsin B staining revealed non-specific localization in the lysosome of cathepsin B. Increasing fluorescence intensity of cathepsin B in the cytoplasm could also be observed, indicating the leakage of cathepsin B from lysosomes into the cytoplasm. Flow cytometry results (Fig. 6c) also confirmed the induction of cell apoptosis after **Py-Tyr** treatment.

The apoptosis mechanism was further investigated by qRT-PCR. A549 cells were treated with **Py-Tyr** for 6, 12 and 24 h and then the RNA expressions of apoptosis executors (Caspase-8 and Caspase-3) and regulator genes (Bcl2 and Bax) were quantified. As shown in Fig. 6d, the RNA expression of the up-stream apoptosis gene Caspase-8, as the initiator of lysosome-associated cell death,[28] and the down-stream apoptosis gene Caspase-3 genes was significantly upregulated upon **Py-Tyr** treatment, while Caspase-3 exhibited a higher level of elevation of expression than Caspase-8. After 24 h's treatment with **Py-Tyr**, the expression of regulator Bax gene was also elevated, while the oncosuppressor gene Bcl2 exhibited downregulation, suggesting a promoting effect on the induced apoptosis. Overall, these results demonstrated that **Py-Tyr** induced lysosome rupture, eventually activating cancer cell apoptosis.

Conclusions

In summary, this study introduces pyrene-capped tyrosine (**Py-Tyr**) as a proof-of-concept molecule in navigating amino acid-based self-assembly for LMP induction and lysosome-targeted cancer therapy. **Py-Tyr** exhibited pH-dependent self-assembling behavior. Under physiological pH, **Py-Tyr** self-assembled into nanoparticles; under acid milieu, **Py-Tyr** was protonated with reduced charge repulsion and these assemblies conglomerated to form micrometer-scaled aggregates. This controlled assembly process, responding specifically to lysosomal acidity, ensured enhanced targeting toward lysosome and effective LMP. Cell experiments results suggested that **Py-Tyr** specifically accumulated in lysosome and caused lysosome rupture, releasing lysosomal contents such as cathepsin B into the cytoplasm. The leakage of cathepsin B eventually activated cell apoptosis, underscoring the therapeutic efficacy of **Py-Tyr** in lysosome-targeted cancer therapy. This study demonstrates amino acid-based self-assembly as a unique and versatile platform for inducing LMP. Further investigations on the screening of amino acids will gain values in realizing its full therapeutic impact.

Materials and methods

Chemicals and instructments

All the solvents and chemicals were commercially available and used as received without further purification. Human lung cancer cell line A549, human liver cancer cell line HepG2, human osteosarcoma cell line Saos2 were purchased from the American Type Culture Collection (ATCC). Dulbecco's modified Eagle medium (DMEM), fetal bovine serum (FBS), and penicillin-streptomycin liquid ($100\times$) were purchased from Gibco (American). Cell Counting Kit-8 (CCK-8) was purchased from Boster Biological Technology Co., Ltd (American). Lysosome-specific staining dyes Lyso-Tracker Red DND-99 and Lyso-Tracker Green DND-26 were purchased from Thermofisher. Cathepsin B Assay Kit (Magic Red) was purchased from Abcam. FTIC-Annexin V/PI Cell apoptosis detection kit was purchased from UElandy.
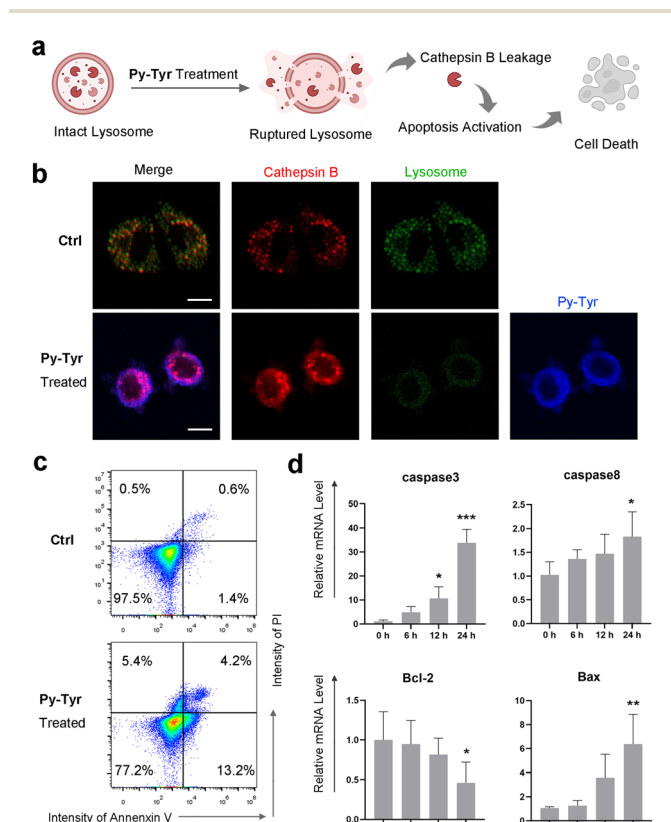

Fig. 6 Lysosome rupture and cell apoptosis induced by **Py-Tyr**. (a) Schematic illustration of induced lysosome rupture and the activation of apoptosis. (b) CLSM images of cathepsin B (red) and lysosomes (green) in the untreated A549 cells of after treatment with 70 μM **Py-Tyr** for 24 h. Fluorescence image of **Py-Tyr** assemblies were also presented (blue). Scale bars represent 10 μm. (c) Flow cytometric analysis of A549 cells apoptosis after treatment with 70 μM **Py-Tyr** for 24 h using FITC–Annexin V and PI co-staining assay. (d) qRT-PCR analysis of apoptosis-related genes in A549 cells treated with 70 μM **Py-Tyr** for 0, 6, 12, and 24 h, mean ± SD, $n = 6$; *$p < 0.05$; **$p < 0.01$; ***$p < 0.001$, respectively.

Mass spectrum was measured by Agilent-6125B mass spectrometer (ESI). 1H spectrum was acquired on a 400 MHz JEOL spectrometer. The ^{1}H NMR chemical shifts (δ) are given in parts per million referring to internal standard tetramethylsilane (TMS). UV-vis spectra were measured on an Ultraviolet-visible Spectrophotometer (YOKE L6). The fluorescence emission spectra were measured on a fluorescence spectrometer (HIACHI F-4700). TEM images were obtained using a Talos L120C transmission electron microscope. The DLS data were obtained using an Anton Paar Litesizer 500, and analysed through OriginPro 2021 Software Student Version (Originlab, Northampton, MA, USA). Fluorescent images were acquired using an LSM FV3000 confocal laser scanning microscope (Olympus, Japan). Cells were analyzed on a Fortessa flow cytometer (BD Biosciences) or on an Aurora spectral cytometer (Cytek). Data were analysed with FlowJo software (Tree Star). qRT-PCR was performed on a QuantGene 9600 real-time PCR (Bioer, Hangzhou, China).

Synthesis of Py-Tyr

Py-Tyr was synthesized by solid phase synthesis on 2-chlorotritylchloride resin (Scheme S1†). Yield 79.8%. ESI-MS (m/z) calcd. for $C_{29}H_{25}NO_4$, 451.1784, found $[M - H]^-$ 450.1161, $[M - 2H]^{2-}$ 248.9437, and $[2M - H]^-$ 901.2345. ^{1}H NMR (400 MHz, methanol-d_4) δ 8.25 (d, $J = 9.3$ Hz, 1H), 8.14 (t, $J = 6.8$ Hz, 2H), 8.11–8.06 (m, 2H), 8.03–7.99 (m, 2H), 7.95 (t, $J = 7.7$ Hz, 1H), 7.79 (d, $J = 7.8$ Hz, 1H), 7.09–7.02 (m, 2H), 6.64 (d, $J = 8.5$ Hz, 2H), 4.60 (dd, $J = 8.9, 4.8$ Hz, 1H), 3.27–3.17 (m, 2H), 3.13 (dd, $J = 14.0, 4.8$ Hz, 1H), 2.92–2.78 (m, 1H), 2.31 (td, $J = 7.1, 2.0$ Hz, 2H), 2.15–1.92 (m, 2H).

UV-vis absorption and fluorescence emission spectroscopy

A stock solution of 20 mM **Py-Tyr** in DMSO was prepared. Prior to the spectral measurement, citrate-phosphate buffer was prepared at different pH values ranging from 4.0 to 8.0. **Py-Tyr** was diluted in citrate-phosphate buffer under different pH values and placed in a quartz cuvette with 1.0 cm path length. UV-vis absorption was measured using a YOKE L6 spectrophotometer. Emission spectra were collected with excitation wavelength of 342 nm. Acquisition settings of 1 nm step size, 0.1 s integration time, and a 350–550 nm scan range were used. The background signal was recorded from blank quartz cuvette and subtracted to obtain each spectrum.

Geometric optimization

The molecular geometry of **Py-Tyr** was optimized using density functional theory (DFT) calculations. The calculation was performed with the GAUSSIAN-09 software package (Gaussian, Inc.), utilizing the B3LYP function.

Dynamic light scattering measurements

Prior to DLS measurement, citrate-phosphate buffer was prepared at different pH values ranging from 4.0 to 8.0. **Py-Tyr** was added to the buffer at a concentration of 100 μM at each pH

and placed in standard test tubes. The DLS data and zeta-potentials were recorded.

Transmission electron microscopy

A drop of 5 μL **Py-Tyr** sample was added on the discharged copper grids coated with thin carbon film for about 60 s. After removing the excess solution with filter paper, the grids were washed with pure water and stained with 1% uranyl acetate for 30 s. The grid was allowed to dry at room temperature and ready for TEM imaging.

Cell culture

HepG2 cells were cultured in ATCC-formulated Eagle's Minimum Essential Medium. Saos2 cells were cultured in ATCC-formulated McCoy's 5a Medium. A549 cells were cultured in ATCC-formulated F-12K Medium. All cells were supplemented with 10% fetal bovine serum (FBS) and 1% penicillin–streptomycin, under a temperature condition of 37 °C. The culture medium is replaced every two days. Cells were maintained in a fully humidified incubator containing 5% CO_2 at 37 °C.

Cell staining

The co-localization of **Py-Tyr** and lysosomes was achieved using confocal laser scanning microscopy. A549 cells were cultured in confocal culture dishes for 24 hours. After the treatment with **Py-Tyr** for 1, 2, 4, 12 and 24 hours, cells were co-stained with Lysotracker to visualize the lysosomes. After staining, the cells were imaged using confocal laser scanning microscopy. Cathepsin B activity was observed using the Magic Red cathepsin B detection kit. Initially, A549 cells were treated with 70 μM **Py-Tyr** for 24 h and co-stained with Magic Red Cathepsin B. Lysosomes were also stained with LysoTracker® Green DND-26 to visualize the localization of cathepsin B. λ_{ex}: 405 nm, λ_{em}: 410–450 nm for **Py-Tyr**, λ_{ex}: 561 nm, λ_{em}: 570–610 nm for LysoTracker® Red DND-99, and λ_{ex}: 488 nm, λ_{em}: 490–530 nm for LysoTracker® Green DND-26, λ_{ex}: 561 nm, λ_{em}: 580–640 nm for cathepsin B, respectively.

Flow cytometry

The apoptosis of A549 cells after **Py-Tyr** treatment was determined using flow cytometry with the FITC-Annexin V/PI cell apoptosis detection kit. A549 cells were treated with **Py-Tyr** at a concentration of 70 μM for 24 hours. After incubation, the cells were resuspended in 400 μL of 1× Annexin V binding buffer and immediately analysed using flow cytometry. FITC-Annexin V was excited by a 488 nm laser, and the fluorescence emission spectrum was detected at 530 nm (FITC channel), while the PI channel emitted fluorescence at approximately 617 nm. In the scatter plot of the bivariate flow cytometer, the lower left quadrant represents live cells (FITC-Annexin V^-/PI^-); the lower right quadrant represents early apoptotic cells (FITC-Annexin V^+/PI^-); the upper right quadrant represents necrotic and late apoptotic cells (FITC-Annexin V^+/PI^+); and the upper left quadrant represents dead cells with disrupted membranes (FITC-Annexin V^-/PI^+).

qRT-PCR

A549 cells were seeded in a 6-well plate at a density of 2×10^5 cells per well. The cells were allowed to adhere by incubating at 37 °C with 5% CO_2 for 12 h. After the incubation with 70 μM **Py-Tyr** for 6, 12, and 24 h, cells were harvested and total RNA was extracted using an RNA Purification Kit (SparkJade, China) following the manufacture's instruction. cDNA was obtained from 500 ng of total RNA using the Reverse Transcription Kit (SparkJade). qRT-PCR was performed using SYBR Green qPCR Master Mix (SparkJade). A two-step method is then used to complete the PCR cycle: Initial denaturation at 94 °C for 2–3 minutes; denaturation at 94 °C for 5–10 seconds; annealing at 55–60 °C for 10–20 seconds; extension at 72 °C for 20–30 seconds. Relative gene expression was calculated using the $2 - \Delta\Delta CT$ method, and β-actin was used as a reference for normalization. The primers were purchased from BioTNT, and primer sequences for Caspase-3, Caspase-8, Bcl2, Bax and β-actin were used as follows:

Caspase-3: 5′-GGAAGCGAATCAATGGACTCTGG-3′(F), 5′-GCATCGACATCTGTACCAGACC-3′(R);

Caspase-8: 5′-TTTCTGCCTACAGGGTCATGC-3′(F), 5′-TGTCCAACTTTCCTTCTCCCA-3′(R);

Bcl2: 5′-ATCGCCCTGTGGATGACTGAGT-3′(F), 5′-GCCAGGA-GAAATCAAACAGAGGC-3′(R);

Bax: 5′-TCAGGATGCGTCCACCAAGAAG-3′(F), 5′-TGTGTCCACGGCGGCAATCATC-3′(R);

β-Actin: 5′-CACCATTGGCAATGAGCGGTTC-3′(F), 5′-AGGTCTTTGCGGATGTCCACGT-3′(R)

Statical analysis

The results are presented as mean and standard deviation, and were obtained from 3–6 independent experiments. Statistical analysis of the data was performed using GraphPad Prism software. When $p > 0.05$, differences were considered non-significant (ns); when $p < 0.05$, differences were considered to be significant (*$p < 0.05$, **$p < 0.01$, ***$p < 0.001$, ****$p < 0.0001$, respectively).

Conflicts of interest

There are no conflicts to declare.

Acknowledgements

References

1 T. Tang, Z.-y. Yang, D. Wang, X.-y. Yang, J. Wang, L. Li, Q. Wen, L. Gao, X.-w. Bian and S.-c. Yu, *Cell Biosci.*, 2020, **10**, 131.

2 S. R. Bonam, F. Wang and S. Muller, *Nat. Rev. Drug Discov.*, 2019, **18**(12), 923–948.

3 W. Trybus, E. Trybus and T. Król, *Int. J. Mol. Sci.*, 2023, **24**(3), 2176.

4 M. Cao, X. Luo, K. Wu and X. He, *Signal Transduct. Targeted Ther.*, 2021, **6**(1), 379.

5 M. Borkowska, M. Siek, D. V. Kolygina, Y. I. Sobolev, S. Lach, S. Kumar, Y.-K. Cho, K. Kandere-Grzybowska and B. A. Grzybowski, *Nat. Nanotechnol.*, 2020, **15**(4), 331–341.

6 C. A. F. Oliveira, L. Ivanova, A. Solhaug and C. K. Fæste, *Mycotoxin Res.*, 2020, **36**(1), 23–30.

7 N. J. Sinha, M. G. Langenstein, D. J. Pochan, C. J. Kloxin and J. G. Saven, *Chem. Rev.*, 2021, **121**(22), 13915–13935.

8 J. S. Li, K. Shi, Z. F. Sabet, W. Fu, H. Zhou, S. Xu, T. Liu, M. You, M. Cao, M. Xu, X. Cui, B. Hu, Y. Liu and C. Chen, *Sci. Adv.*, 2019, **5**(9), eaax0937.

9 G. Li, X. Hu, P. Nie, D. Mang, S. Jiao, S. Zhang, S. R. Roy, S. Yukawa, S. Asahina, H. Sugasawa, W. Cortes, Z. Zhou and Y. Zhang, *Nano Lett.*, 2021, **21**(1), 747–755.

10 J. Song, Q. Zhang, G. Li and Y. Zhang, *Langmuir*, 2022, **38**(29), 8733–8747.

11 G. Li, X. Hu, X. Wu and Y. Zhang, *Nano Lett.*, 2021, **21**(7), 3052–3059.

12 M. T. Jeena, L. Palanikumar, E. M. Go, I. Kim, M. G. Kang, S. Lee, S. Park, H. Choi, C. Kim, S.-M. Jin, S. C. Bae, H. W. Rhee, E. Lee, S. K. Kwak and J.-H. Ryu, *Nat. Commun.*, 2017, **8**(1), 26.

13 B. Jana, S. Jin, E. M. Go, Y. Cho, D. Kim, S. Kim, S. K. Kwak and J.-H. Ryu, *J. Am. Chem. Soc.*, 2023, **145**(33), 18414–18431.

14 D. Kim, S. Kim, G. Park, H. Choi and J.-H. Ryu, *JACS Au*, 2022, **2**(11), 2539–2547.

15 J. Wang, L. Hu, H. Zhang, Y. Fang, T. Wang and H. Wang, *Adv. Mater.*, 2022, **34**(1), 2104704.

16 C. Wu, C. Wang, T. Zhang, G. Gao, M. Wei, Y. Chen, X. Li, F. Wang and G. Liang, *Adv. Healthcare Mater.*, 2022, **11**(1), 2101346.

17 S. J. Bird and J. B. Lloyd, *Cell Biochem. Funct.*, 1995, **13**(2), 79–83.

18 C. Ménard-Moyon, V. Venkatesh, K. V. Krishna, F. Bonachera, S. Verma and A. Bianco, *Chem.–Eur. J.*, 2015, **21**(33), 11681–11686.

19 D. Zaguri, T. Kreiser, S. Shaham-Niv and E. Gazit, *Molecules*, 2018, **23**(6), 1273.

20 C. Tang, A. M. Smith, R. F. Collins, R. V. Ulijn and A. Saiani, *Langmuir*, 2009, **25**(16), 9447–9453.

21 J. Wang, Q. Dang, Y. Gong, Q. Liao, G. Song, Q. Li and Z. Li, *CCS Chem.*, 2021, **3**(12), 274–286.

22 M. J. Frisch, G. W. Trucks, H. B. Schlegel, G. E. Scuseria, M. A. Robb, J. R. Cheeseman, G. Scalmani, V. Barone, B. Men-nucci, G. A. Petersson, H. Nakatsuji, M. Caricato, X. Li, H. P. Hratchian, A. F. Izmaylov, J. Bloino, G. Zheng, J. L. Sonnen-berg, M. Hada, M. Ehara, K. Toyota, R. Fukuda, J. Hasega-wa, M. Ishida, T. Nakajima, Y. Honda, O. Kitao, H. Nakai, T. Vreven, J. A. Montgomery Jr, J. E. Peralta, F. Ogliaro, M. Bearpark, J. J. Heyd, E. Brothers, K. N. Kudin, V. N. Staroverov, T. Keith, R. Kobayashi, J. Normand, K. Raghavachari, A. Rendell, J. C. Burant, S. S. Iyengar, J. To-masi, M. Cossi, N. Rega, J. M. Millam, M. Klene, J. E. Knox, J. B. Cross, V. Bakken, C. Adamo, J. Jaramillo, R. Gomperts, R. E. Stratmann, O. Yazyev, A. J. Austin, R. Cammi, C. Pomelli,

J. W. Ochterski, R. L. Martin, K. Morokuma, V. G. Zakrzewski, G. A. Voth, P. Salvador, J. J. Dannenberg, S. Dapprich, A. D. Daniels, O. Farkas, J. B. Foresman, J. V. Ortiz, J. Cioslowski and D. J. Fox, *Gaussian.*, 2013.

23 J. J. Rennick, A. P. R. Johnston and R. G. Parton, *Nat. Nanotechnol.*, 2021, **16**, 266.

24 M. S. de Almeida, E. Susnik, B. Drasler, P. Taladriz-Blanco, A. Petri-Fink and B. Rothen-Rutishauser, *Chem. Soc. Rev.*, 2021, **50**, 5397.

25 M. Okada, A. Matsuzawa, A. Yoshimura and H. Ichijo, *J. Biol. Chem.*, 2014, **289**(47), 32926–32936.

26 S. Aits and M. Jäättelä, *J. Cell Sci.*, 2013, **126**(9), 1905–1912.

27 Z. Xie, M. Zhao, C. Yan, W. Kong, F. Lan, Narengaowa, S. Zhao, Q. Yang, Z. Bai, H. Qing and J. Ni, *Cell Death Dis.*, 2023, **14**(4), 255.

28 B. Zhong, M. Liu, C. Bai, Y. Ruan, Y. Wang, L. Qiu, Y. Hong, X. Wang, L. Li and B. Li, *Mol. Ther.*, 2020, **28**(4), 1078–1091.